



Misorientation and grain boundary orientation dependent grain boundary response in polycrystalline plasticity

Tuncay Yalçinkaya¹ · İzzet Özdemir² · İzzet Tarik Tandoğan¹

Received: 15 April 2020 / Accepted: 30 December 2020 / Published online: 5 February 2021
© The Author(s), under exclusive licence to Springer-Verlag GmbH, DE part of Springer Nature 2021

Abstract

This paper studies the evolution of intergranular localization and stress concentration in three dimensional micron sized specimens through the Gurtin grain boundary model (J Mech Phys Solids 56:640–662, 2008) incorporated into a three dimensional higher-order strain gradient crystal plasticity framework (Yalçinkaya et al. in Int J Solids Struct 49:2625–2636, 2012). The study addresses continuum scale dislocation-grain boundary interactions where the effect of crystal orientation mismatch and grain boundary orientation are taken into account through the grain boundary model in polycrystalline metallic specimens. Due to the higher-order nature of the model, a mixed finite element formulation is used to discretize the problem in which both displacements and plastic slips are considered as primary variables. For the treatment of grain boundaries within the solution algorithm, an interface element is formulated and implemented together with the bulk plasticity model. The capabilities of the framework is demonstrated through 3D polycrystalline examples considering grain boundary conditions, grain boundary strength, the orientation distribution and the specimen size. A detailed grain boundary condition and stress concentration analysis is presented. The advantages and the disadvantages of the model is discussed in detail through numerical examples.

Keywords Strain gradient plasticity · Microforming · Size effect · Grain boundary · Crystal plasticity

1 Introduction

The recent developments in the production of miniaturized devices increase the demand for micro-components where the thickness ranges from tens to hundreds of microns (see e.g. [1,2]). At this length scale, many challenges exist such as size effect and stress concentrations at the grain boundaries, due to plasticity activity at the grain boundaries and the orientation mismatch (see e.g. [3–10]). Various metallic alloys, e.g. aluminum, exhibit substantial localization and stress concentration at the grain boundaries during microforming (see e.g. [11–15]). Therefore, inter-granular damage evolution is a prominent failure mechanism at this length scale, yet it is not straightforward to include physical localization mechanisms of grain boundaries into (crystal) plasticity finite

element simulations. Crystal plasticity approach captures the intrinsic evolution of deformation heterogeneity in metallic materials developing due to crystal orientation mismatch. Theoretically, it is expected that crystal plasticity simulations would give good match for the plastic deformation evolution in each grain and at the grain boundaries with the experimental findings due its ability to describe the link between the crystallographic slip and plastic deformation. However, except for a couple of recent works (e.g. [16] obtained up to 80% agreement for Ti–6Al–4V), [17] show good correlation for Tantalum oligocrystal), the studies generally could not present quantitative agreements of crystal plasticity simulations with experimental observations on the spatial evolution of deformation even for the samples with restricted number of grains (see e.g. [18–24]). They could mostly mention a well agreement on the statistical response of a polycrystalline aggregates through comparison with EBSD and DIC measurements. While in many cases the differences were attributed to the constant friction condition in the simulations, some authors explicitly stated the importance of the grain boundaries and their orientation on the spatial evolution of stress and strain (see e.g. [25]). However, the compli-

✉ Tuncay Yalçinkaya
yalcinka@metu.edu.tr

¹ Department of Aerospace Engineering, Middle East Technical University, 06800 Ankara, Turkey

² İzmir Institute of Technology, Faculty of Engineering, Department of Civil Engineering, 35430 Urla, İzmir, Turkey

cated hardening behavior of the grain boundaries is ignored in crystal plasticity simulations. Our recent experience for the comparison of classical (local) crystal plasticity finite element simulations with experimental micro-DIC results did not give promising results either for aluminum alloys. Especially for the cases with a moderate number of grains, the local behavior is quite different between numerical and experimental results (see e.g. [11]). Some other studies focus on the effect of other microstructural features for such differences. For instance, Luccarelli et al. [26] address the effect of carbides on the evolution of strain fields, and it was illustrated that without the addition of carbides, it was not possible to obtain matching results from the polycrystal plasticity finite element simulations. There are many other studies that show the restricted capability of crystal plasticity modeling of the spatial strain evolution. Therefore the investigations should concentrate more on the reason for such discrepancies. A way to increase the capabilities of the polycrystal plasticity simulations is to take into account the hardening behavior of grain boundaries considering the orientation of the grain boundary and the crystallographic misorientation of the neighboring grains, which is addressed in detail in the current study.

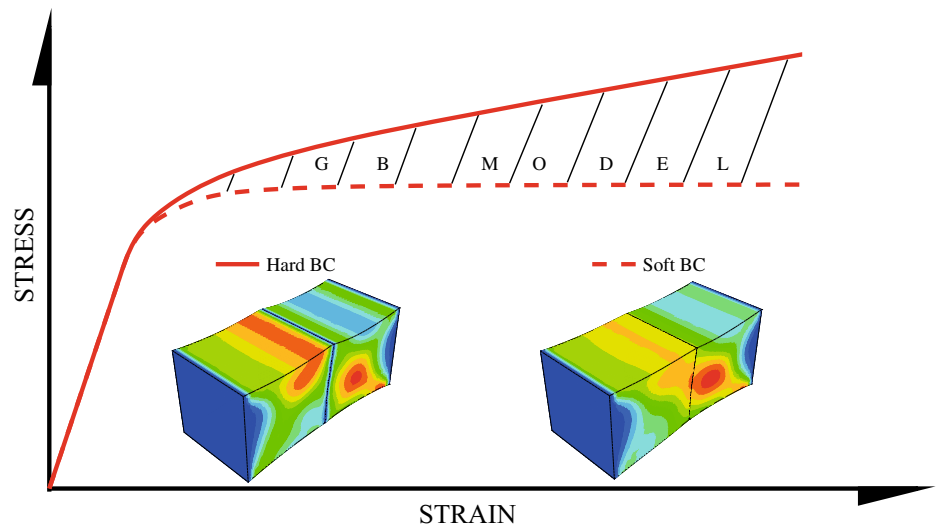
Grain boundary modeling in crystal plasticity withdrew substantial interest after the theoretical contribution by Gurtin [27], where the energetic behavior of the grain boundary is governed by a grain boundary tensor, which describes the effect of orientation mismatch and the orientation of the grain boundary. Özdemir and Yalçinkaya [28] were the first to incorporate this formulation into a strain gradient crystal plasticity model developed in [29,30] as a 2D coupled framework in terms of plastic slips and displacements and tested its performance on bi-crystal specimens. Then a more detailed analysis is presented by Özdemir and Yalçinkaya [31] in three dimensional setting for bi-crystals. In the meanwhile, there have been other studies addressing this issue in crystal plasticity using both Gurtin formulation and other similar approaches. van Beers et al. [32] developed a model addressing both dissipative and energetic character of the grain boundary and illustrated the effect of mis-orientation in bi-crystals in plane strain setting. Later on, van Beers et al. [33] obtained the grain boundary energy from atomistic simulations. Gottschalk et al. [34] performed a detailed theoretical and numerical investigation of Gurtin [27] in a cubic polycrystal composed of cubic grains. Bayerschen et al. [35] presented a comprehensive overview on the geometric criteria used in both experiments and computational models, focusing on continuum approaches. In addition to geometric GB models based on the misorientation of the grains and the orientation of the grain boundary, there have been models developed for the grain boundary hardening based on interface yield condition and surface considerations (see e.g. [36,37]).

Using a grain boundary model based on the geometrical description of orientation mismatch is a simple way of reflect-

ing coarse grained response of dislocation-grain boundary interactions at the grain boundaries. In this way, instead of using classical boundary conditions for plastic deformation in strain gradient crystal plasticity theory, which do not even exist in local crystal plasticity models, one can capture the behavior between limiting cases of micro-free and micro-hard boundary conditions (see Fig. 1 for the illustration). In higher order non-local crystal plasticity models, a field related to plastic deformation (e.g. dislocation density in [38], plastic slip in [39] or plastic slip gradients in [40]) enters the finite element formulation as a degree of freedom in addition to displacements. Even though such variables on each slip system increases the number of unknowns and the size of the tangent matrix substantially, it gives the possibility of direct calculation of the gradients through shape function derivatives, which makes the model non-local and more efficient in terms of mesh dependence and convergence. Moreover, we are able to define boundary conditions, e.g. for plastic slips, as in the current work (see e.g. also [41,42] for some discussions on the issue). Defining a zero slip conditions at the (grain) boundaries would block the transmission of dislocations from one grain to the other one, or a traction free condition would make the grain boundaries ‘disconnected’ as far as slip is concerned and the slips (dislocations) reaching to the grain boundary do not ‘feel’ any resistance, please see Fig. 1 for the illustration in terms of plastic slip. However, in reality, the dislocation-grain boundary interaction is quite complicated with many physical mechanisms occurring at the same time, and these boundary conditions do not reflect the plasticity mechanisms at the grain boundaries properly. From continuum perspective having a geometric grain boundary model with a strength variable allows to tune the inter-granular microstructure evolution that would give responses in between the limiting cases as shown in Fig. 1. Such an approach would offer the opportunity for crystal plasticity community to do more flexible simulations and to obtain better match with experimental results. In this context, the purpose of the current study is to illustrate this phenomenon in polycrystalline materials in 3D micron sized specimens prepared with Voronoi tessellation, which has not been addressed previously in the open literature. Even though we do not conduct experimental comparison analysis in the current state, the model offers a great potential for users to do more realistic simulations for the the evolution of localization and stress concentration, which has been a great challenge as discussed previously.

The paper is organized as follows. First, in Sect. 2, the formulations of both strain gradient crystal plasticity and the grain boundary model are addressed in a thermodynamical setting. Then the finite element implementation of both models as user finite element subroutines is studied. In Sect. 4, the numerical examples are presented where different aspects of the model are illustrated in polycrystalline specimens.

Fig. 1 Stress versus strain representation together with slip contours within a crystallographically misaligned bi-crystal under uni-axial loading through limiting GB conditions: soft (micro-free) and hard (micro clamped)



Finally, the work is summarized and concluding remarks are given in Sect. 5.

2 Strain gradient crystal plasticity framework and grain boundary model

In this section, the polycrystalline plasticity framework is addressed within the continuum thermodynamics context, covering both bulk and interface behavior separately. The balance relations are obtained through the principle of virtual power, followed by the consideration of second law of thermodynamics and constitutive assumptions for consistency. The strain gradient crystal plasticity framework is a higher-order model where crystallographic slip is considered to be a degree of freedom in addition to displacement field. Therefore both bulk and interface plasticity behavior is built on plastic slip field, in terms of which the additional boundary conditions can be defined. Such a framework requires two balance relations in the bulk part, i.e. a classical macroscopic force balance for the solution of displacements and a microscopic balance relation for the solution of plastic slip field, and further relations at the interface in terms of plastic slip at both sides of the grain boundary.

2.1 Macroscopic and microscopic force balance relations

Since the main focus of the study is the orientation mismatch based localization at the grain boundaries, the bulk plasticity behavior is kept rather simple for a clear illustration of the interface plasticity effects. Therefore the crystal plasticity framework is developed in the small strain setting, where the time dependent displacement field of a body with a grain

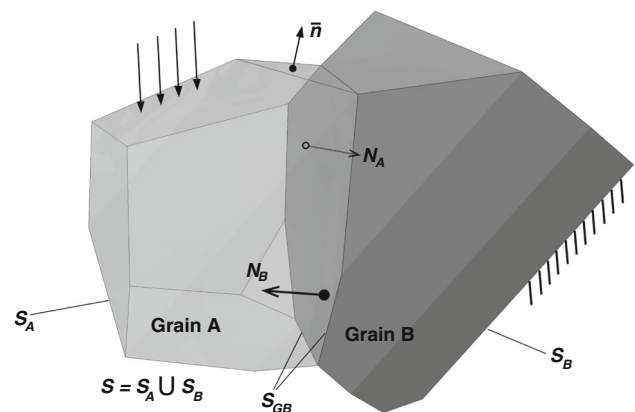


Fig. 2 The grain boundary representation in a two-grain body

boundary, as shown in Fig. 2, is denoted by $u = u(x, t)$, where x indicates the position of a material point. Note that in this study the displacement field is continuous across the grain boundary. The separation of the interfaces is not considered, and the focus is concentrated on the plastic localization and stress concentrations at the grain boundaries. However, some recent studies have addressed the mechanical opening phenomenon at the grain boundaries through cohesive zone elements (see e.g. [8,10,43]). Furthermore, although the upcoming discussions are based on a two grain body as depicted in Fig. 2, the derivations are valid for bodies composed of multiple grains. The strain tensor ϵ is defined as $\epsilon = 1/2(\nabla u + (\nabla u)^T)$, and the velocity vector is represented as $v = \dot{u}$. The strain is decomposed additively as $\epsilon = \epsilon^e + \epsilon^p$ into an elastic part ϵ^e and a plastic part ϵ^p . The plastic component of the strain tensor is calculated through the summation of plastic slip rates on each slip systems, $\dot{\epsilon}^p = \sum_{\alpha} \dot{\gamma}^{\alpha} P^{\alpha}$ with $P^{\alpha} = \frac{1}{2}(s^{\alpha} \otimes m^{\alpha} + m^{\alpha} \otimes s^{\alpha})$

representing the symmetrized Schmid tensor, where s^α and m^α are the unit slip direction vector and unit normal vector on slip system α , respectively. A set, composed of elastic strain tensor ϵ^e , plastic slips γ^α and gradient of plastic slips $\nabla\gamma^\alpha$ on system α is chosen to be the set of state variables. Then the arguments of Gurtin (e.g. [44,45]) is followed for the derivation of force balances through principle of virtual power. In a classical macroscopic system, the traction $t(\bar{n})$ expends power over the velocity \dot{u} and stress σ expends power over the elastic strain-rate $\dot{\epsilon}^e$. In the microscopic system considered in this study a scalar microscopic stress π^α expends power over the slip rate on each slip system $\dot{\gamma}^\alpha$, a vector of microscopic stress ξ^α expends power over the slip-rate gradient $\nabla\dot{\gamma}^\alpha$, a scalar microscopic traction $\chi^\alpha(\bar{n})$ expends power over $\dot{\gamma}^\alpha$ and finally a scalar interfacial microscopic grain boundary stress λ^α expends power over the grain boundary slip rates $\dot{\gamma}_A^\alpha$ and $\dot{\gamma}_B^\alpha$, where approaching the grain boundary from different grains are designated by subscripts A and B. All the virtual rates are collected in the generalized virtual velocity field $\mathcal{V} = (\delta\dot{u}, \delta\dot{\epsilon}^e, \delta\dot{\gamma}^\alpha, \delta\dot{\gamma}_A^\alpha, \delta\dot{\gamma}_B^\alpha)$ which satisfy $\nabla\delta\dot{u} = \delta\dot{\epsilon}^e + \delta\dot{\omega} + \sum_\alpha \delta\dot{\gamma}^\alpha s^\alpha \otimes m^\alpha$, where $\dot{\omega}$ represents the rate of rotation. By setting $\delta\dot{\gamma}^\alpha = 0$ and enforcing the virtual power balance, the classical linear momentum balance

$$\nabla \cdot \sigma = 0. \tag{1}$$

and the traction condition

$$t(\bar{n}) = \sigma \bar{n} \tag{2}$$

are obtained. A similar approach is followed for the derivation of the microscopic counterparts of the relations. Setting this time $\delta\dot{u} = 0$ and enforcing virtual power balance leads to the microscopic force balance inside the bulk material on each slip system α ,

$$\tau^\alpha - \pi^\alpha + \nabla \cdot \xi^\alpha = 0 \tag{3}$$

the micro scale traction condition on the outer boundary of the bulk material

$$\chi^\alpha(\bar{n}) = \xi^\alpha \cdot \bar{n} \tag{4}$$

and microscopic grain boundary interface conditions on both sides of the grain boundary

$$\begin{aligned} \xi_A^\alpha \cdot N^A &= \lambda_A^\alpha \\ \xi_B^\alpha \cdot N^B &= \lambda_B^\alpha \text{ or } -\xi_B^\alpha \cdot N^A = \lambda_B^\alpha \end{aligned} \tag{5}$$

where the equality $N^A = -N^B$ is used to write the last expression for λ_B^α . The strong forms of the fundamental balance laws are converted to weak forms and

used in the finite element implementation together with the boundary/interface conditions derived above. However, no constitutive assumption or relation has been presented yet, which will be covered in the next section following the arguments of continuum thermodynamics.

2.2 Free energy imbalance for bulk and interface

For the description of the material behavior of the higher-order strain gradient crystal plasticity model, the 2nd law of thermodynamics is considered here for a thermodynamically consistent framework. Note that this is not the only way to develop advanced crystal plasticity models. There are a number of examples which do not follow the thermodynamics but base their formulation on the physics of the plasticity phenomenon at micron scale focusing on the relations for the internal stress fields due to individual dislocations and the evolution of dislocation densities (see e.g. [38,46–49]). In here the model is developed in terms of plastic slips on each slip system and the complicated physical relations for the internal stresses and GND evolution are not included directly, nevertheless the dislocation density evolution could be post-processed upon need. For the purpose of clarity the relations are kept as simple as possible. The starting point is the dissipation inequality, which should be satisfied and could be written in terms of internal power P_i and the free energy ψ as,

$$D = P_i - \dot{\psi} = \sigma : \dot{\epsilon}^e + \sum_\alpha (\pi^\alpha \dot{\gamma}^\alpha + \xi^\alpha \cdot \nabla \dot{\gamma}^\alpha) - \dot{\psi} \geq 0. \tag{6}$$

The free energy of the material is assumed to depend only on the elastic strain and the gradient of the plastic slip, which is directly related to the geometrically necessary dislocation density,

$$\psi(\epsilon^e, \nabla\gamma^\alpha) = \psi_e(\epsilon^e) + \psi_{\nabla\gamma}(\nabla\gamma^\alpha). \tag{7}$$

In this way GND evolution is considered to be fully energetic. Through the establishment of the stress tensor $\sigma = \frac{d\psi_e}{d\epsilon^e}$, and the microstress vectors $\xi^\alpha = \frac{\partial\psi_{\nabla\gamma}}{\partial\nabla\gamma^\alpha}$, the simpler form of the reduced dissipation inequality is obtained where π^α has the only dissipative contribution,

$$D = \sum_\alpha (\pi^\alpha) \dot{\gamma}^\alpha \geq 0 \text{ or } D = \sum_\alpha \sigma_{dis}^\alpha \dot{\gamma}^\alpha \geq 0 \tag{8}$$

and the stress terms multiplying the plastic slip rates are recognized as the set of dissipative stresses σ_{dis}^α defined as $\sigma_{dis}^\alpha = \pi^\alpha$. In order to satisfy the inequality at the slip system level, the following relations are suggested,

$$\sigma_{dis}^\alpha = \varphi^\alpha \text{sign}(\dot{\gamma}^\alpha) \text{ and } \varphi^\alpha = s^\alpha (|\dot{\gamma}^\alpha|/\dot{\gamma}_0^\alpha)^m \tag{9}$$

by which the thermodynamical consistency is obtained in a simple way. In order to focus solely on the influence of the grain boundary effects, the actual slip resistance, s^α , is considered to be constant here. The self and latent hardening phenomena could be incorporated using classical relations. m and $\dot{\gamma}_0^\alpha$ are the strain rate sensitivity exponent and the reference slip rate, respectively. Restating the microforce balance in an alternative form, i.e. $\pi^\alpha = \tau^\alpha + \nabla \cdot \xi^\alpha$ and using Eq. (9) leads to

$$\text{sign}(\dot{\gamma}^\alpha) \frac{s^\alpha}{(\dot{\gamma}_0^\alpha)^m} |\dot{\gamma}^\alpha|^m = \tau^\alpha + \nabla \cdot \xi^\alpha \tag{10}$$

which can also be put into the following form,

$$\dot{\gamma}^\alpha = \dot{\gamma}_0^\alpha \left(\frac{|\tau^\alpha + \nabla \cdot \xi^\alpha|}{s^\alpha} \right)^{1/m} \text{sign}(\tau^\alpha + \nabla \cdot \xi^\alpha) \tag{11}$$

Quadratic relations are used for the elastic free energy ψ_e and the plastic slip gradients free energy contribution $\psi_{\nabla\gamma}$, i.e.

$$\begin{aligned} \psi_e &= \frac{1}{2} \boldsymbol{\varepsilon}^e : {}^4\mathbf{C} : \boldsymbol{\varepsilon}^e \\ \psi_{\nabla\gamma} &= \sum_\alpha \frac{1}{2} A \nabla \gamma^\alpha \cdot \nabla \gamma^\alpha \end{aligned} \tag{12}$$

with ${}^4\mathbf{C}$ representing the 4th order elasticity tensor and A is the scalar quantity, which includes an internal length scale parameter, governing the non-locality of the model. In here it is expressed as $A = ER^2/(16(1 - \nu^2))$, where R describes the radius of the dislocation domain contributing to the internal stress field, ν is Poisson’s ratio and E is Young’s modulus. Note that the free energy functions enter the slip evolution equation through $\tau^\alpha = \frac{d\psi_e}{d\boldsymbol{\varepsilon}^e} : \mathbf{P}^\alpha$ and $\xi^\alpha = \frac{\partial \psi_{\nabla\gamma}}{\partial \nabla \gamma^\alpha}$. The gradient part of the energy is the surface energy term, increasing with the large value of the internal length scale parameter R , which would induce a large internal stress and therefore penalize high plastic slip gradients, spreading the geometrically necessary dislocation densities. Without a specific grain boundary model, which is addressed next, the internal length scale parameter, therefore the internal stresses are the main driving force of the localization occurring at the grain boundaries. In such a framework only the limiting boundary conditions (see Fig. 1), hard (zero-slip) and soft (traction free), for the plastic slips could be described and R governs microstructure evolution at the grain boundaries. However in the current model, a specific grain boundary model is employed whose constitutive behavior is characterized by a grain boundary free energy term that includes a grain boundary strength parameter which is amplified with the orientation mismatch of neighboring grains and the orientation of the grain boundary. Therefore grain boundary

localization is not only affected by the boundary conditions and the internal length scale parameter, but also with the grain boundary strength, mis-orientation and grain boundary orientation. The details are presented in the following. Similar to the bulk behavior, the discussion of the grain boundary model starts with the thermodynamics, where the dissipation related with the GB can be written in terms of grain boundary power P_{GB} and the associated free energy ψ_{GB} as,

$$\begin{aligned} D_{GB} &= P_{GB} - \dot{\psi}_{GB} \\ &= \sum_\alpha \int_{S_{GB}} (\lambda_A^\alpha \dot{\gamma}_A^\alpha + \lambda_B^\alpha \dot{\gamma}_B^\alpha) dS - \dot{\psi}_{GB} \geq 0 \end{aligned} \tag{13}$$

A free energy function ψ_{GB} is required that would depict the coarse grained representation of complex grain boundary-dislocation slip interaction mechanism such as dislocation transmission, emission and dissociation of dislocations within the grain boundary. Several experimental and computational studies have revealed that the constitutive behavior of grain boundaries governed by the local features such as grain misorientation and GB orientation. Motivated by the underlying physics of non-coherent slip systems of neighboring grains, a GB model that accounts for essential geometrical features presented in [27] is adopted in this work. The authors previously studied the model on bi-crystals (see [28,31]) and presented the preliminary results for polycrystals in proceedings (see [8,50]) but a detailed study in 3D polycrystalline metallic materials have not been presented before, which is the purpose of current work. This step requires tremendous effort to pre-process the finite element model where the microstructure is prepared and the grain boundary elements are inserted between the grains and to post-process where the Abaqus results are converted into proper odb files for the detailed analysis. Such technical implementation details are not discussed here. In [27], the slip incompatibility of the neighboring grains is described in terms of the grain boundary Burgers tensor defined as,

$$\mathbf{G} = \sum_\alpha [\gamma_B^\alpha s_B^\alpha \otimes \mathbf{n}_B^\alpha - \gamma_A^\alpha s_A^\alpha \otimes \mathbf{n}_A^\alpha] (\mathbf{N} \times) \tag{14}$$

where for any vector \mathbf{N} , $\mathbf{N} \times$ is the tensor with components $(\mathbf{N} \times)_{ij} = \varepsilon_{ikj} N_k$. The Burgers tensor given in Eq. (14), describes both the relative misorientation of the grains and the orientation of the grain boundary. Furthermore, the magnitude of grain boundary Burgers tensor is expressed in terms of slip interaction moduli ($C_{AA}^{\alpha\beta}$, $C_{AB}^{\alpha\beta}$ and $C_{BB}^{\alpha\beta}$) as follows,

$$|\mathbf{G}|^2 = \sum_\alpha \sum_\beta (C_{AA}^{\alpha\beta} \gamma_A^\alpha \gamma_A^\beta + C_{BB}^{\alpha\beta} \gamma_B^\alpha \gamma_B^\beta + -2C_{AB}^{\alpha\beta} \gamma_A^\alpha \gamma_B^\beta) \tag{15}$$

In this formulation $C_{AA}^{\alpha\beta}$ and $C_{BB}^{\alpha\beta}$ represent the interactions between slip systems within grain A and grain B respectively, and therefore they are called intra-grain interaction moduli, whereas $C_{AB}^{\alpha\beta}$ represent the interaction between slip systems of the two grains and called inter-grain interaction moduli. For their explicit forms and for a detailed discussion on the physical meaning of the interaction-moduli, the reader may consult to Özdemir and Yalçinkaya [28,31] that focus on simple 2D and bi-crystal examples in an illustrative way. A simple free energy function of the following form is adapted here, ignoring the dissipative effects,

$$\psi_{GB} = \frac{1}{2}\kappa|\mathbf{G}|^2 \tag{16}$$

where κ is a positive constant modulus, which represents the strength of the grain boundary itself. If there is misorientation between the neighbouring grains, there will be a contribution to the grain boundary free energy which will be amplified with the multiplier κ . The microstructure evolution around the grain boundary is therefore directly affected by the grain boundary free energy, as well as with the internal length scale parameter. This gives the freedom to tune the microstructure evolution and the localization around the grain boundaries with a fixed value of internal length scale parameter. Inserting ψ_{GB} into the dissipation inequality leads to the following relations for the microscopic grain boundary stress terms,

$$\begin{aligned} \lambda_A^\alpha &= \kappa \sum_{\beta} \left(\gamma_A^\beta C_{AA}^{\alpha\beta} - \gamma_B^\beta C_{AB}^{\alpha\beta} \right) \\ \lambda_B^\alpha &= \kappa \sum_{\beta} \left(\gamma_B^\beta C_{BB}^{\alpha\beta} - \gamma_A^\beta C_{BA}^{\alpha\beta} \right). \end{aligned} \tag{17}$$

where the difference between the slips are being penalized by the grain boundary strength κ . Grain boundary may act as a soft ($\kappa = 0$) or hard ($\kappa = \infty$) boundary as long as there is a mismatch between the grain orientations. In this way the behavior of the grain boundary is not restricted to the limiting cases and the response between soft and hard boundaries can be obtained. In the next section, the finite element implementation of the framework for both bulk and interface part is discussed in short.

3 Finite element implementation

The initial boundary value problem in hand consists of two coupled balance equations for which a mixed finite element formulation is opted. Linear momentum and the microscopic force balance equations are solved in a monolithic manner resulting in the two primary fields, namely, the displacements \mathbf{u} and the plastic slips γ^α . Note that internal variable formalism is exploited in local plasticity (see e.g. [51,52]) and the

lower order strain gradient frameworks (see e.g. [20,53–56]) where the balance equations are solved for only the nodal displacements and plastic variables evolve locally and are stored as history variables at every material point, i.e. Gauss point in a finite element context. On the other hand, higher order models, as utilized here, treat plasticity specific variables, such as dislocation densities (see e.g. [38,47,48]) and plastic slips (see e.g. [29,30,57,58]) as nodal degree freedoms, which allow straight forward calculation of the gradients of the plastic field. Mixed finite element formulation developed here starts with the strong form of the balance equations,

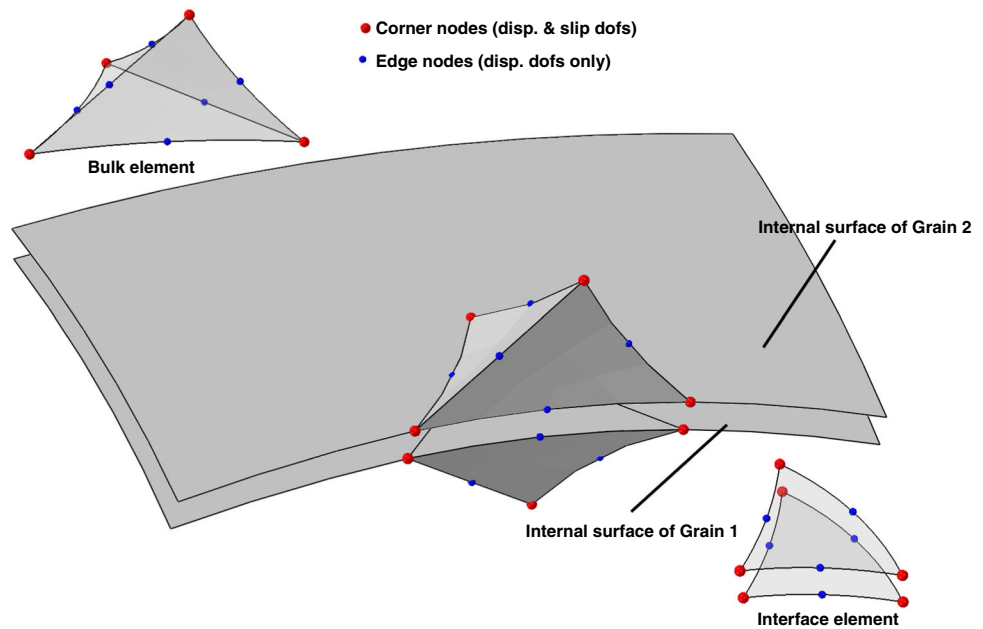
$$\begin{aligned} \nabla \cdot \boldsymbol{\sigma} &= \mathbf{0} \\ \text{sign}(\dot{\gamma}^\alpha) \frac{s^\alpha}{(\dot{\gamma}_0^\alpha)^m} |\dot{\gamma}^\alpha|^m - \tau^\alpha - \nabla \cdot \boldsymbol{\xi}^\alpha &= 0 \end{aligned} \tag{18}$$

complemented by the boundary conditions (2), (4) on the associated outer boundaries and the interface conditions (5) on the grain boundary, respectively. In order to obtain the weak forms, balance equations are multiplied by weighting functions $\delta \mathbf{u}$ and $\delta \gamma^\alpha$ and integrated over the domain Ω , resulting in,

$$\begin{aligned} G_u &= \int_{\Omega} \nabla \delta \mathbf{u} : \boldsymbol{\sigma} d\Omega - \int_S \delta \mathbf{u} \cdot \mathbf{t} dS \\ G_\gamma^\alpha &= \int_{\Omega} \text{sign}(\dot{\gamma}^\alpha) \delta \gamma^\alpha |\dot{\gamma}^\alpha|^m d\Omega \\ &\quad - \int_{\Omega} \frac{(\dot{\gamma}_0^\alpha)^m}{s^\alpha} \delta \gamma^\alpha \tau^\alpha d\Omega \\ &\quad + \int_{\Omega} \frac{(\dot{\gamma}_0^\alpha)^m}{s^\alpha} \nabla \delta \gamma^\alpha \cdot \mathbf{A} \nabla \gamma^\alpha d\Omega \\ &\quad - \int_S \frac{(\dot{\gamma}_0^\alpha)^m}{s^\alpha} \delta \gamma^\alpha \chi^\alpha dS \\ &\quad - \int_{S_{GB}} \frac{(\dot{\gamma}_0^\alpha)^m}{s^\alpha} \delta \gamma_A^\alpha \lambda_A^\alpha dS \\ &\quad - \int_{S_{GB}} \frac{(\dot{\gamma}_0^\alpha)^m}{s^\alpha} \delta \gamma_B^\alpha \lambda_B^\alpha dS \end{aligned} \tag{19}$$

The external traction vector \mathbf{t} on the external boundary S is the forcing term for the first equation whereas grain boundary tractions (λ_A & λ_B) and $\chi^\alpha = \mathbf{A} \nabla \gamma^\alpha \cdot \mathbf{n}$ are driving the evolution of slip within the domain. Following a standard Galerkin approach (Bubnov-Galerkin), the same interpolations are used for unknown fields and their associated weighting functions. A quadratic interpolation for displacements and a linear one for slips are embedded within a 10-noded tetrahedral element primarily due to its potential advantage in meshing of complicated 3D poly-crystalline geometries. For a typical 10-noded tetrahedra shown in Fig. 3, the slip dofs are defined only at the corner nodes whereas a quadratic displacement interpolation requires displacement dofs at every node of the element. This element type is utilized to model

Fig. 3 Finite element representation for both interface and bulk parts



the elasto-plastic behaviour of grains for which 5 slip systems (all of them are octahedral slip systems, please see Table 1), of a face centered cubic (fcc) crystal are used. All fcc slip systems could be considered as well in the numerical examples, but that would increase the computational cost (with 15 dofs at the corner nodes and 78 dofs in total for an element) without affecting the qualitative conclusions drawn here. Zero thickness interface elements with 12 nodes are inserted along the grain boundaries (please see Fig. 3) which essentially facilitates the integration of the grain boundary contributions appearing in the weak form. These elements enable one to access the slip values along the grain boundary either approached from grain A or grain B. However it is worth mentioning that the interface elements are mechanically fully intact and does not cause any discontinuity in the displacement field. During the solution phase, same nodal displacements at the corresponding nodes of an interface element are enforced by means of equality constraints (rigid ties). Furthermore, 12-noded interface element suits well to potential extensions of the framework, in particular, injection of mechanical decohesion of grain boundaries described by traction-separation relations, see e.g. [10]. For the temporal discretization of $\dot{\gamma}^\alpha$, backward Euler integration scheme is employed which simply approximates $\dot{\gamma}^\alpha$ by $\dot{\gamma}^\alpha \approx [\gamma_{n+1}^\alpha - \gamma_n^\alpha]/\Delta t$ with $\Delta t = t_{n+1} - t_n$. Intermediate steps and the explicit forms of the discretized bulk and interface integrals are available in [31]. Newton–Raphson solution procedure is used to solve the discretized balance equations which require consistent linearization. After linearization, the following set of linear equations are obtained,

Table 1 Slip systems used in the bulk elements

Slip system	\mathbf{n}	\mathbf{s}
1	$\frac{1}{\sqrt{2}}[\bar{1} 1 0]$	$\frac{1}{\sqrt{3}}(1 1 1)$
2	$\frac{1}{\sqrt{2}}[1 0 \bar{1}]$	$\frac{1}{\sqrt{3}}(1 1 1)$
3	$\frac{1}{\sqrt{2}}[0 \bar{1} 1]$	$\frac{1}{\sqrt{3}}(1 1 1)$
4	$\frac{1}{\sqrt{2}}[1 \bar{1} 0]$	$\frac{1}{\sqrt{3}}(\bar{1} \bar{1} 1)$
5	$\frac{1}{\sqrt{2}}[0 1 1]$	$\frac{1}{\sqrt{3}}(\bar{1} \bar{1} 1)$

$$\begin{bmatrix} \underline{K}^{uu} & \underline{K}^{u\gamma} \\ \underline{K}^{\gamma u} & \underline{K}^{\gamma\gamma} + \underline{K}_{GB}^{\gamma\gamma} \end{bmatrix} \begin{bmatrix} \Delta \underline{u} \\ \Delta \underline{\gamma}^\alpha \end{bmatrix} = \begin{bmatrix} -\underline{R}^u + \underline{R}_u^{ext} \\ -\underline{R}^\gamma + \underline{R}_\gamma^{ext} \end{bmatrix} \quad (20)$$

which are solved for the corrective unknowns $\Delta \underline{u}$ and $\Delta \underline{\gamma}^\alpha$. \underline{K}^{uu} , $\underline{K}^{u\gamma}$, $\underline{K}^{\gamma u}$ and $\underline{K}^{\gamma\gamma}$ are the global tangent matrices of the bulk whereas $\underline{K}_{GB}^{\gamma\gamma}$ represents the contribution of the interface elements to the system tangent stiffness matrix. The difference between the global internal force columns \underline{R}^u & \underline{R}^γ and the external force columns \underline{R}_u^{ext} & $\underline{R}_\gamma^{ext}$ tend to zero through this iterative procedure. For relatively small m values and polycrystals with large number of grains, a difficulty in convergence especially at the early stages of loading is observed. To circumvent this problem, after some tests, $\text{sign}(\dot{\gamma}^\alpha)$ function is approximated by $\tanh(k \dot{\gamma}^\alpha)$ where k is a large positive constant, typically chosen in the order of modulus of elasticity.

4 Numerical examples

In this section the numerical performance of the model is illustrated through different microstructural parameters on micron size specimens with different number of grains. The simulations are conducted for a cylindrical specimen with length of 100 μm and diameter of 25 μm under uniaxial tension as well as with diameter and length of 25 μm under uniaxial tension and shear loading. The examples with 5, 10, 100, 250, 500 and 600 grains are considered where the material parameters presented in Table 2 are employed. The specimens are loaded with displacement at one end while they are fully constrained (encastre) at the other end. Since the imposed restriction results in stress concentration at the boundary, an additional case with symmetry conditions is presented to address the influence of boundary conditions. Moreover, while at the ends of the specimen hard boundary is assumed for plastic slip the remaining surfaces considered to be soft, and the conditions at the grain boundaries are discussed in detail.

Initially a uniaxial specimen with 10 randomly oriented grains is considered. The engineering stress versus strain responses for different rate sensitivity parameters, m , are plotted in Fig. 4 considering different κ values together with the classical limiting boundary conditions to have a comparison with the approaches without the grain boundary model and to evaluate the capability of the current framework. Note that in qualitative strain gradient polycrystalline plasticity models, it is common to assume a viscous form of the slip equation with $m = 1$ (see e.g. [28,59]) for numerical efficiency. In this study different values of the exponent is considered and studied in detail. The rate exponent influences clearly the onset of plastic deformation which is deferred with increasing value. Large values of m induce lower macroscopic yield strength, yet it does not influence the discussions on the effect of grain boundary strength κ as shown in Fig. 4. In the current as well as in the upcoming examples for $m = 1$ cases reference slip rate is considered to be $\dot{\gamma}_0 = 0.115$. The case with $\kappa = 0$ is identified to be the soft boundary condition, which is different than the micro-free boundary conditions in the strain gradient crystal plasticity literature (see e.g. [60–62]), which is illustrated in the same plot as well. In those frameworks since there is no interface element, the traction free boundary condition cannot be imposed. In case of so-called micro-free boundary conditions of these aforementioned studies, the resulting slip distribution is continuous between the grains which in turn implies a non-zero (slip associated) traction on the grain boundaries. This actually introduces a harder condition than the real soft boundary condition that is captured here with a zero stiffness grain boundary element, which is shown in the same plots where the classical soft boundary (micro-free) condition results in more hardening than the case with $\kappa = 0$. Another lim-

iting case in the literature is the hard boundary condition, which is referred to as micro-clamped boundary condition where the plastic slips are set to zero. It is clearly observed in Fig. 4 that with the increasing value of the interface strength the behavior of the material approaches to hard boundary condition. However the situations in between the two limiting cases are obtained as well, which is not possible in the models without a grain boundary model. In reality no complete soft or hard boundary condition would exist at the grain boundaries of deforming polycrystals. There would be complicated grain boundary-dislocation interaction mechanisms which are obtained with the current grain boundary model through the interface strength κ at an upper scale. In the same figure the unloading response of the model is presented for the case of soft boundary conditions where an elastic unloading response is observed.

Next, the spatial stress evolution is discussed for the same example. Initially the influence of grain boundary strength is presented in Fig. 5 for different κ values, i.e. $\kappa = 0, 5$ and 20. Due to the mismatch in the grain orientations, which are taken completely random, there is certain stress concentration at the grain boundaries even for the soft case with $\kappa = 0$. These concentrations increase substantially with increasing κ . At the inner parts of the specimen at certain locations there are considerable differences in terms of stress concentration between the soft ($\kappa = 0$) and the high κ cases. In the frequently used local crystal plasticity frameworks, which do not incorporate a grain boundary model, there would be only one response for the stress distribution which would be closer to the soft case, leading to various problems in the experimental comparison studies. However, the current framework presents a great potential in capturing more realistic response at both micro and macro scales due to the freedom supplied by the grain boundary strength for tuning the response with respect to experimental observations. Therefore, in the future validation studies, this parameter will play a key role. Furthermore, In Fig. 6 the responses for the soft ($\kappa = 0$), micro-free and hard boundary conditions are presented for different rate sensitivity exponent values, i.e. $m = 1$ and $m = 0.1$. There is a huge difference between soft and hard grain boundary cases which correspond to free dislocation movement from one grain to the other and complete blockage of the dislocation transfer through the grain boundary. The stress levels reach to very high values especially at the grain boundaries for the hard cases. Note there is a substantial influence of m on the stress distribution for soft case with $\kappa = 0$, while the differences are observed to be much less for the other cases. Serious stress concentrations occur at the end of the specimens where encastre boundary condition is applied. This is completely due to the restriction coming from the boundary conditions affecting mostly the outer part of the specimen. This issue will be discussed in the next examples in the context of symmetry boundary conditions.

Table 2 Material properties of the strain gradient crystal plasticity model

Young modulus E (MPa)	Poisson ratio ν (-)	Reference slip rate $\dot{\gamma}_0$ (s^{-1})	Slip resistance s (MPa)	Orientations ($^\circ$)	Material length scale R (μm)
70000.0	0.33	0.001	25.0	Random	0.4

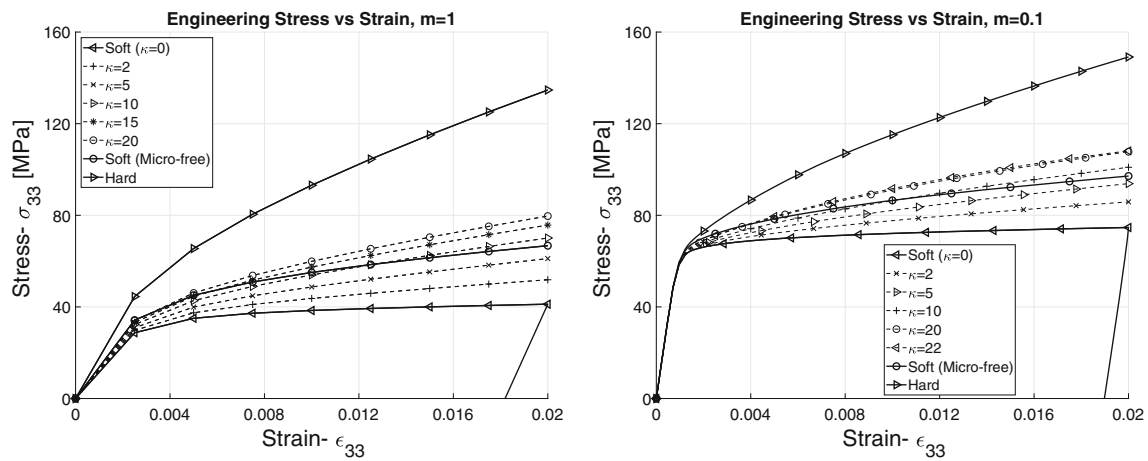


Fig. 4 Engineering stress versus strain response for a 10 grain specimen through different grain boundary strength κ values in comparison to classical grain boundary conditions for $m = 1$ (left) and $m = 0.1$ (right)

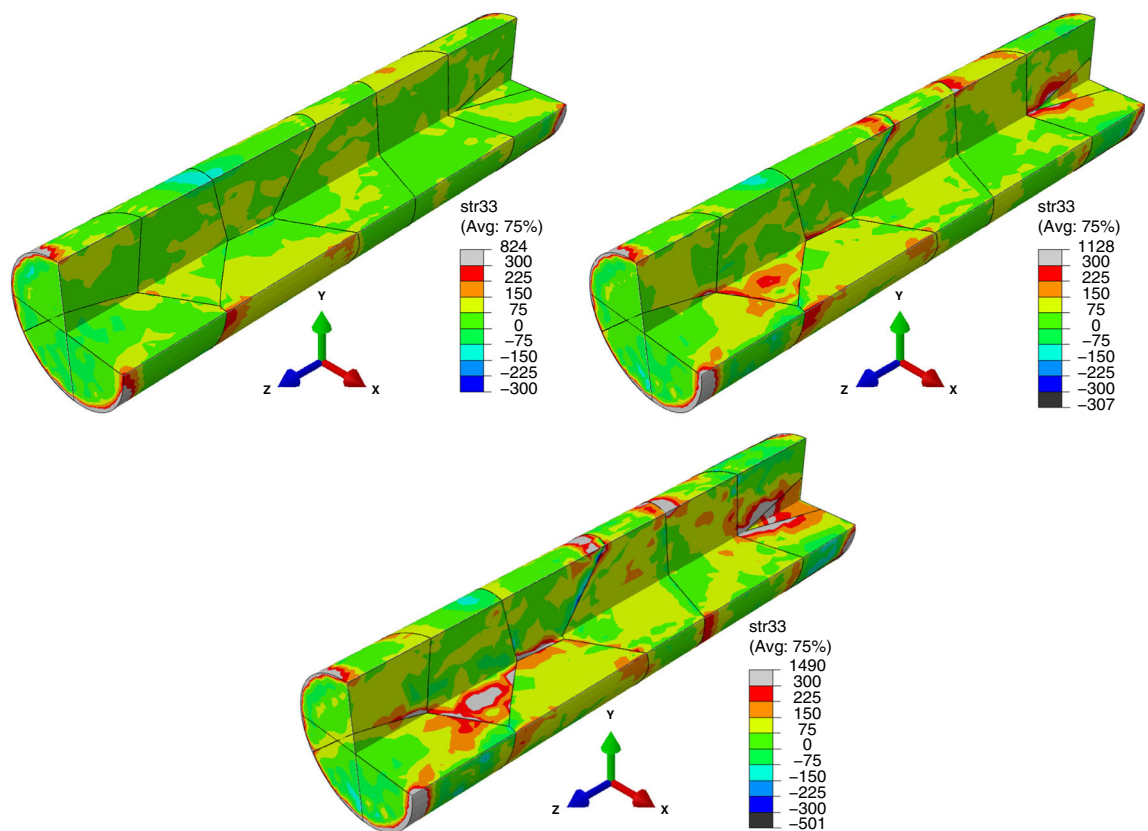


Fig. 5 Stress distribution for $\kappa = 0$ (top-left), $\kappa = 5$ (top-right), $\kappa = 20$ (bottom) values of the grain boundary strength in specimens with 10 randomly oriented grains for $m = 0.1$ under 2% tensile strain

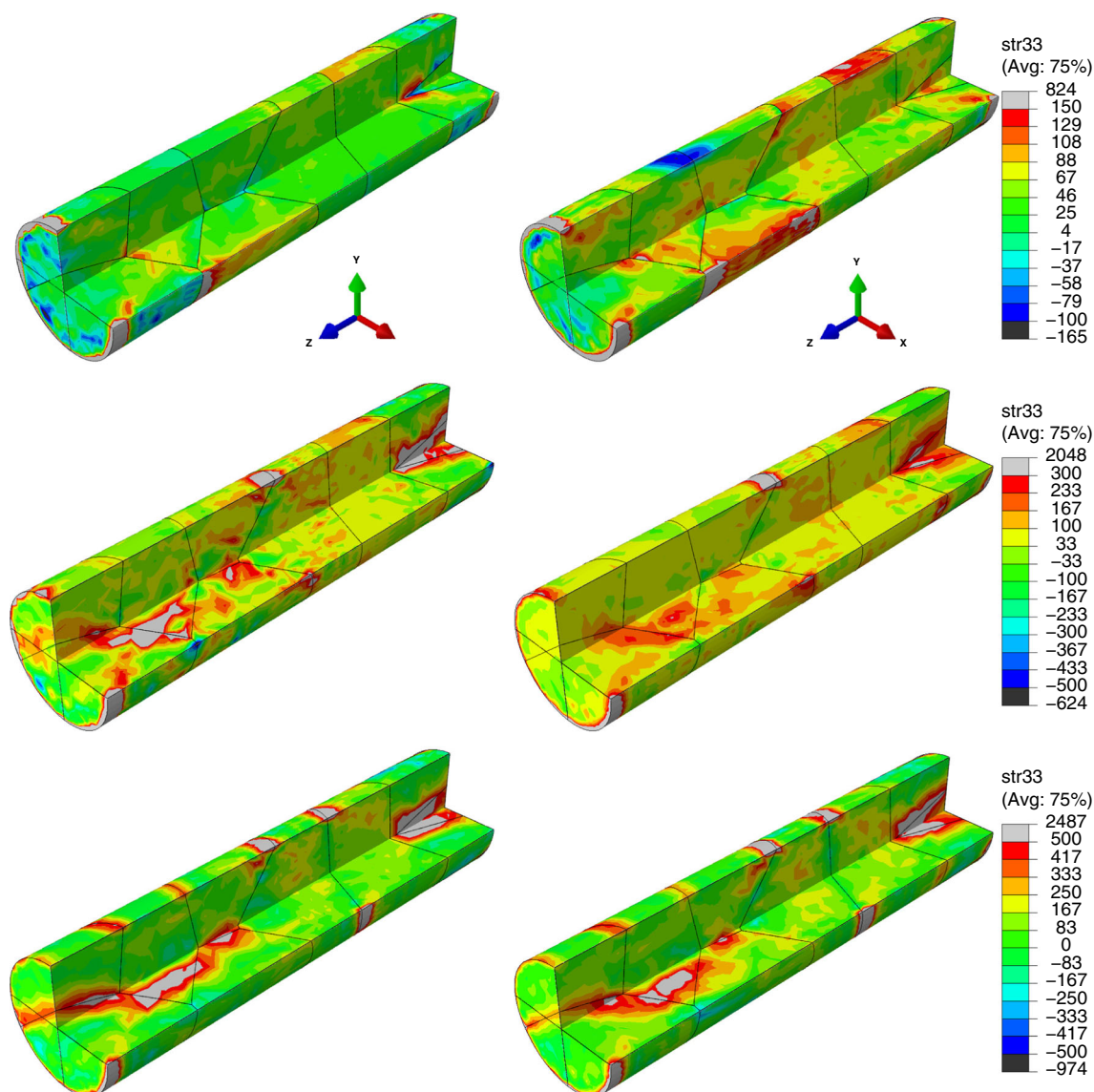


Fig. 6 Stress distribution for soft ($\kappa = 0$) (top), soft (micro-free) (middle), hard (bottom) grain boundary conditions in specimens with 10 randomly oriented grains under 2% tensile strain. Effect of strain rate sensitivity exponent m is compared: $m = 1$ (left) and $m = 0.1$ (right)

In Fig. 7 the stress and strain distribution upon unloading is presented for $\kappa = 0$ and $m = 0.1$ in the same specimen. Even though the average stress value is zero, there are certain spots with stress concentrations in the specimen when macroscopic force returns to zero. Moreover, due to elastic unloading, pronounced strain values are observed throughout the specimen.

In the next example the specimens with symmetry boundary conditions are addressed in Figs. 8 and 9, where the displacements are applied at both ends of the quarter specimen in $+z$ and $-z$ directions while the faces perpendicular to x and y are constrained in the x and y directions respectively. As shown previously in Figs. 5, 6 and 7 the applied boundary conditions induce stress concentrations at the ends of

the specimens, which will disappear here upon applied symmetry conditions. In this context, the influence of κ value for the stress concentrations and plastic slip evolution is discussed in specimens with 252 randomly oriented grains in Figs. 8 and 9. A symmetric grain structure is not physical indeed, however the results and discussions are identical for the full specimens without any symmetry. Moreover, without the boundary induced stress concentrations the illustration becomes more clear. In Fig. 8 the effect of κ is shown for $m = 0.2$. For the soft boundary case with $\kappa = 0$ low level inter-granular stress concentrations occur throughout the specimen due to the orientation mismatch. Only a couple of grain boundaries at the middle section of the specimen show substantial stress concentrations due to high degree of

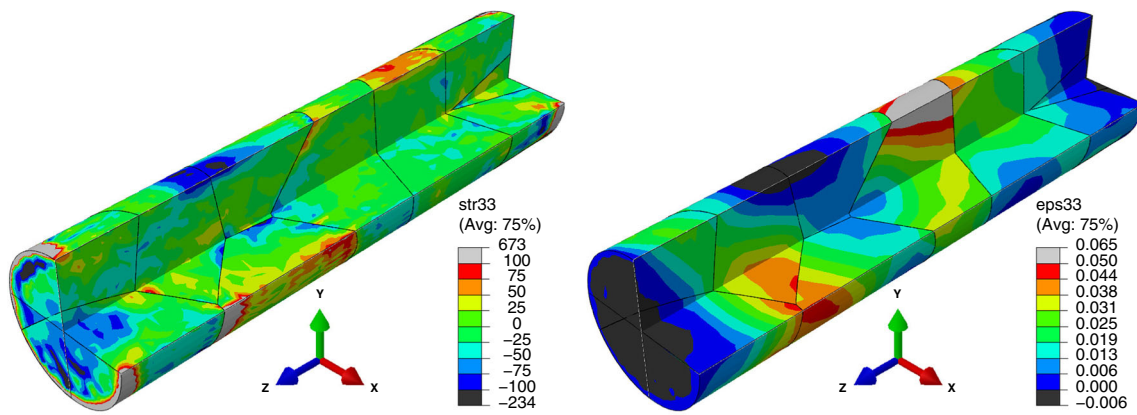


Fig. 7 Stress (left) and strain (right) distribution for $\kappa = 0$ value of the grain boundary strength in specimens with 10 randomly oriented grains for $m = 0.1$, upon unloading when macroscopic force returns to zero

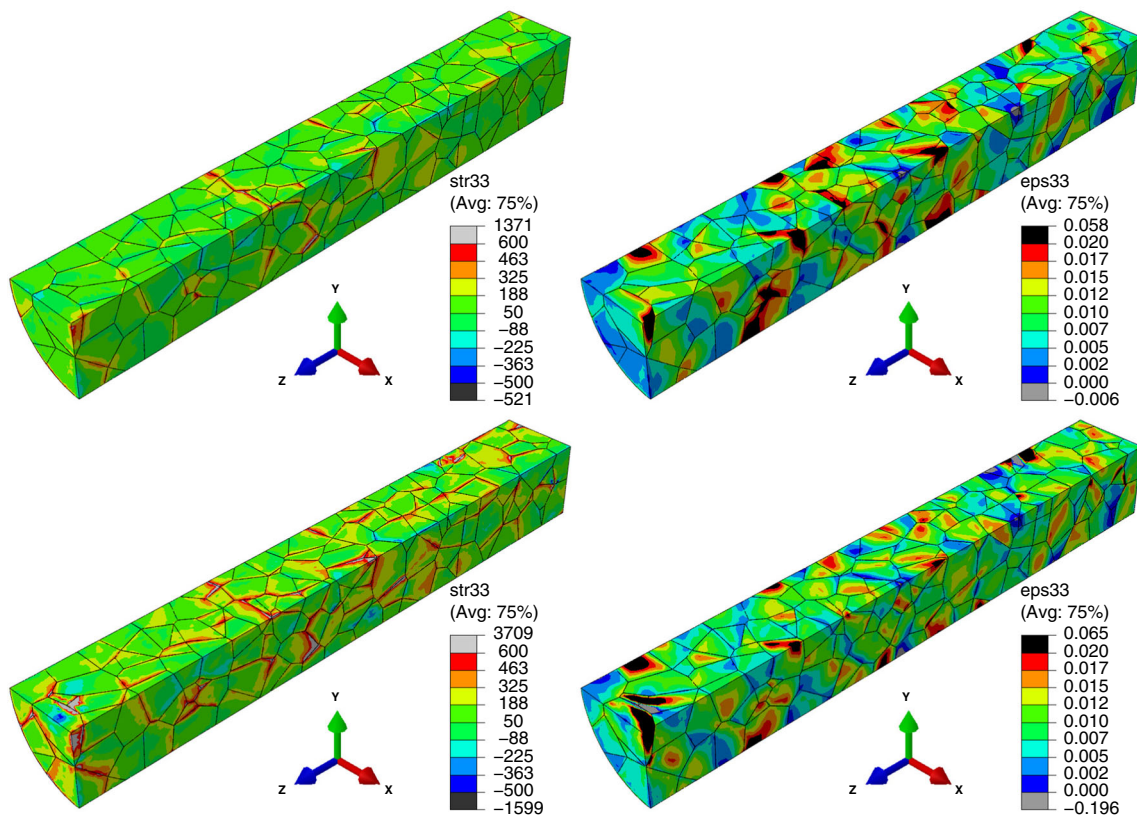


Fig. 8 Stress (left) and strain (right) distribution for $\kappa = 0$ (upper), $\kappa = 16$ (lower) for $m = 0.2$ in specimens with 252 randomly oriented grains at 1% tensile strain in z-direction

orientation mismatch. The level of stress at all grain boundaries increases remarkably for $\kappa = 16$ which is reflected also on the macroscopic yielding and hardening as discussed previously. There are significant differences in the evolution of strain field as well which is illustrated in the same figure on the right side. In Fig. 9 the plastic slip evolution is shown for the same κ and m values. A completely different slip evolution is observed for different slip systems. In each case, while the plastic slip γ evolves throughout the grain with notice-

able values at the grain boundaries for low κ , the evolution is rather confined to the grain interiors with increasing grain boundary strength.

Next, the effect of the misorientation is addressed, where the Euler angles of the grain orientations are restricted to have values between 40° and 45° in a specimen with 100 grains. In this way, the misorientation between the grains is reduced and the grain boundary strength, κ is expected to have less effect than the previous case where it was multiplied with higher

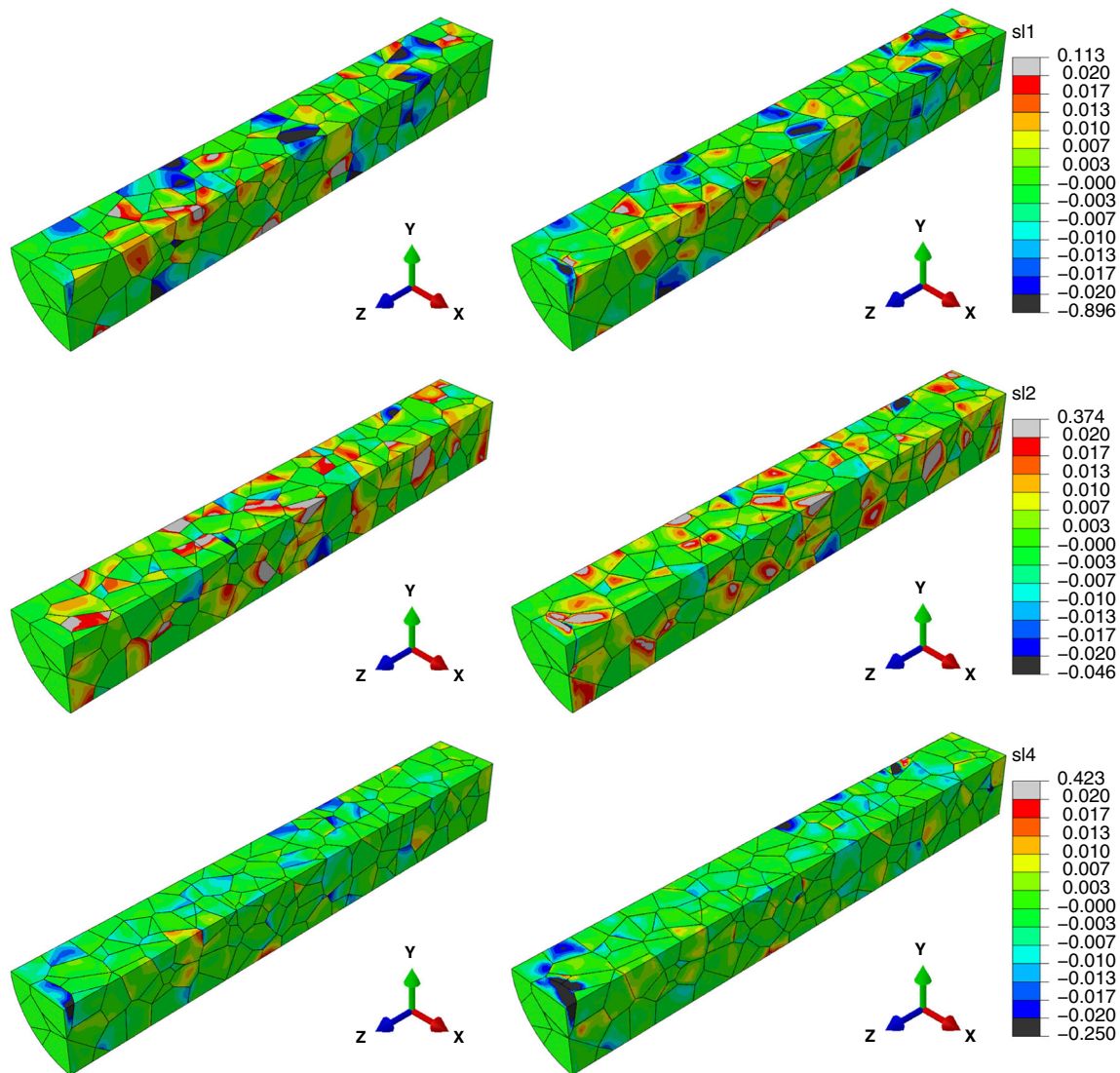


Fig. 9 Slip contours for $\kappa = 0$ (left) and $\kappa = 16$ (right) in 3 different slip systems for $m = 0.2$ in specimens with 252 randomly oriented grains at 1% tensile strain in z -direction. From top to bottom Slip-1, Slip-2, and Slip-4 evolution are shown in order

values in the free energy function due to the high misorientation. Moreover, while in the previous examples the stress concentration locations evolved randomly, a more regular pattern is expected to occur in this case. In Fig. 10 the spatial distribution of stress is illustrated for $\kappa = 0, 8$ and 20 and $m = 0.2$ at 2% macroscopic strain. The stress concentration and localization align according to the given crystallographic orientation of the grains, which are magnified with increasing values of grain boundary strength. However due to the restricted misorientation values it requires higher κ values to get comparable stress concentrations with respect to the previous example. In Fig. 11 the stress-strain responses for different κ values are illustrated for both the randomly oriented case and the case where the orientations are restricted between 40° and 45° . The difference in the macroscopic con-

stitutive response between the $\kappa = 0$ and $\kappa = 4.5$ cases is substantially higher for the randomly oriented grains than the microstructure with restricted orientations. This result shows that grain boundary strength has higher influence for the specimen with higher misorientations as expected from the formulation resulting in more pronounced localization and stress concentrations at the grain boundary.

Figure 12 shows the influence of the κ for a higher range of values from 0 to 1000 in comparison to classical boundary conditions for the same example with orientations restricted to the values between 40° and 45° and $m = 0.2$. A smooth convergence to hard boundary condition is obtained with increasing κ . However, in randomly distributed orientation examples numerical problems might occur for high values of κ depending on the orientation distribution and rate sensi-

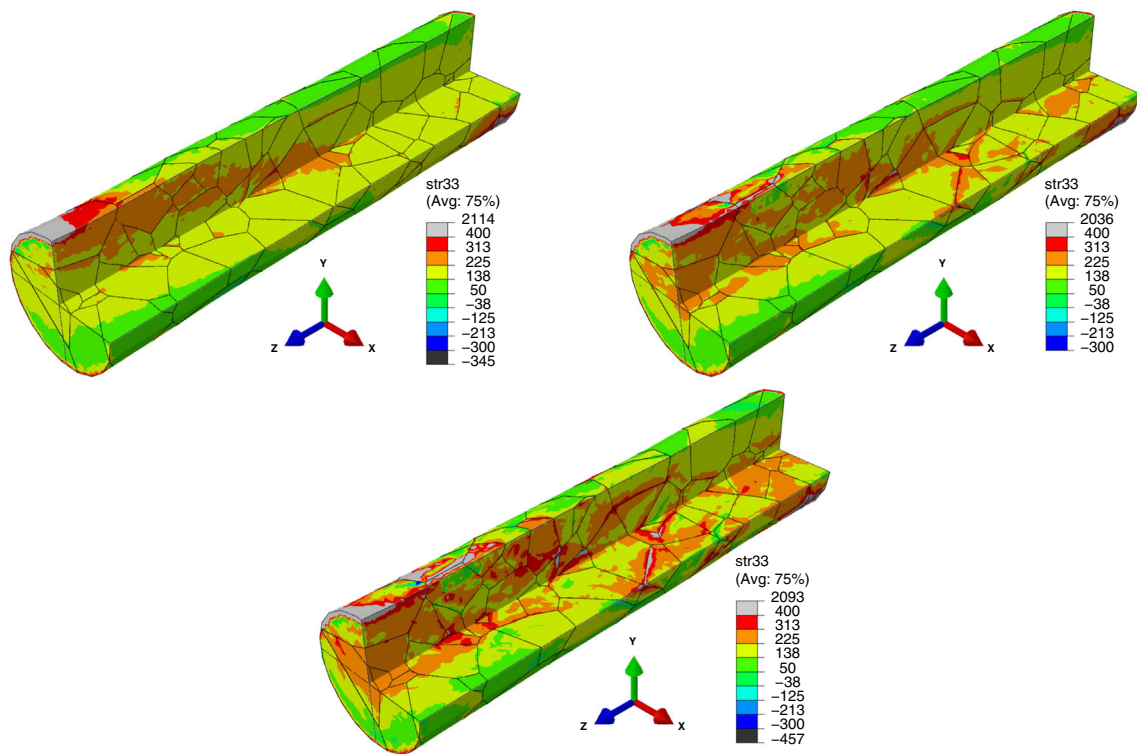


Fig. 10 Stress distribution for $\kappa = 0$ (upper left), $\kappa = 8$ (upper right) and $\kappa = 20$ (lower) in specimens with 100 randomly oriented grains with angles restricted between $40^\circ - 45^\circ$ for $m = 0.2$ under 2% tensile strain in z-direction

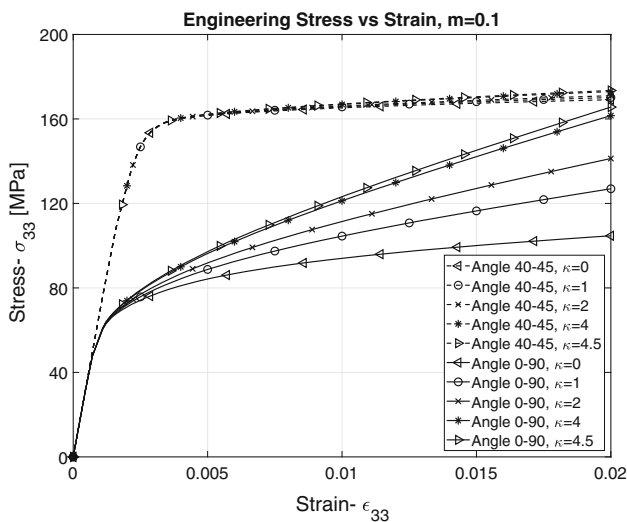


Fig. 11 Engineering stress versus strain curve for different κ values in a randomly oriented specimen (dashed line) and in a specimen where the orientation mismatch is restricted (continuous line) for $m = 0.1$

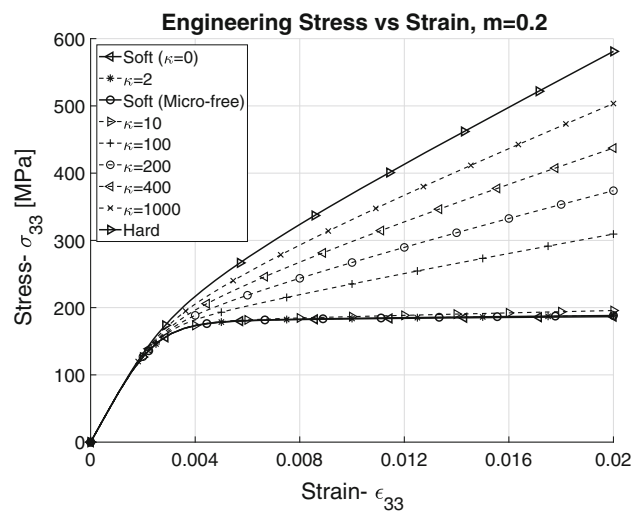


Fig. 12 Engineering stress versus strain curve for different κ values in a specimen where the orientations are restricted between 40° and 45° for $m = 0.2$

tivity exponent, where nonphysical results, i.e. exaggerated localization might occur. Therefore one has to be careful with selecting this parameter and it does not always approach to hard boundary condition case smoothly. Note also that in this example both soft boundary conditions, micro-free and $\kappa = 0$, converge to each other due to the lack of misorien-

tation. In fact the soft boundary case with $\kappa = 0$ behaves almost like a micro-free boundary condition.

The influence of the grain (crystal) orientation distribution is discussed in a specimen with 600 randomly oriented grains for constant grain boundary strength $\kappa = 3$ and $m = 1$. The distribution of stress and strain is illustrated in Fig. 13 where a

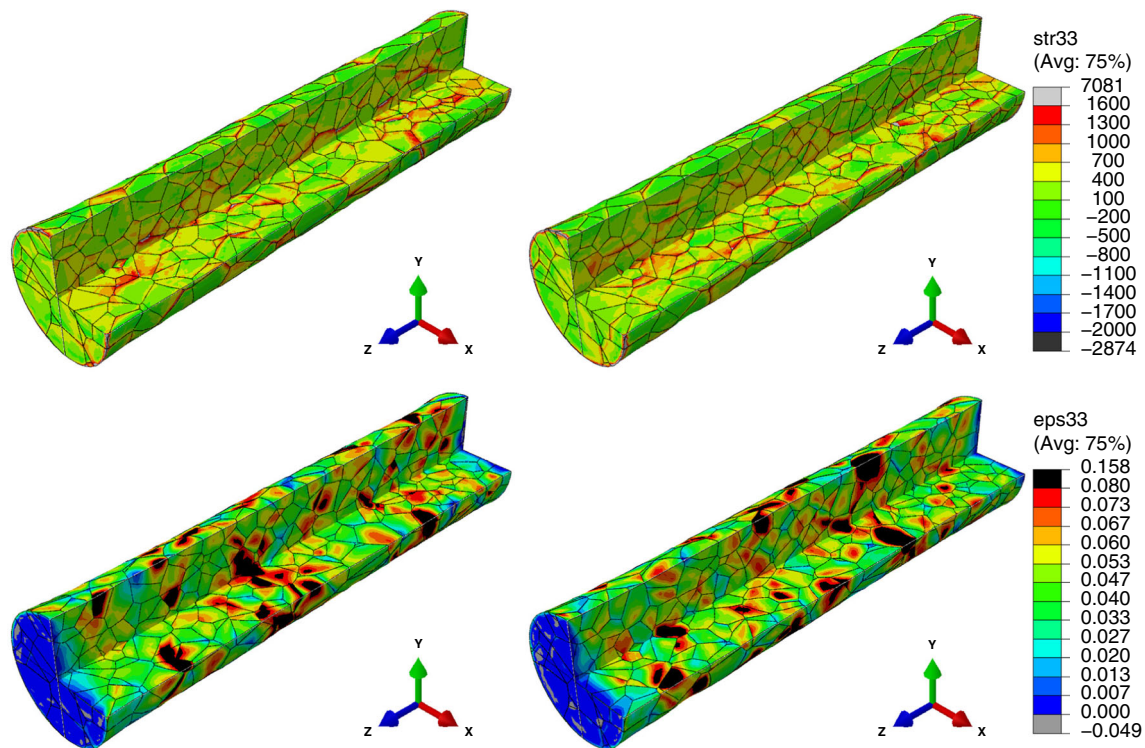


Fig. 13 Stress (upper) and strain (lower) distributions for $\kappa = 3$ and $m = 1$, for 8% strain in z-direction where the same orientation set is distributed randomly: distribution 1 (left) and 2 (right)

random orientation set is distributed differently in each case. Naturally, the microstructure evolution and the stress concentrations at the grain boundaries are completely different in each case. In this way, the same grain morphology with the same pole figure results in different microstructure evolution. Due to the high number of grains a statistical size effect is not obtained at macro scale even though there are considerable differences at micron level. In other words, both specimen has the same macroscopic stress versus strain response.

Next, the size effect is discussed shortly. In Fig. 14 two types of size effects are shown together. For the illustration of the extrinsic (statistical) size effect, specimens with same size but with different number of grains are considered, i.e. 5, 100 and 500. For each case different orientation sets are assigned and a huge scatter is obtained in stress-strain response for the specimen with 5 grains. The orientation of individual grains affects the constitutive response substantially, resulting in such a size effect. The observed scatter decreases with increasing number of grains and approaches to isotropic response eventually. In the meanwhile, when the number of grains is increased in the same specimen, naturally the grain size decreases. Therefore the intrinsic size effect works at the same time (Hall–Petch effect) and the case with smaller grain size shows stronger response. For the case with 500 grains, which has the smallest grain size, the dislocations have more chance to meet a grain boundary than the other

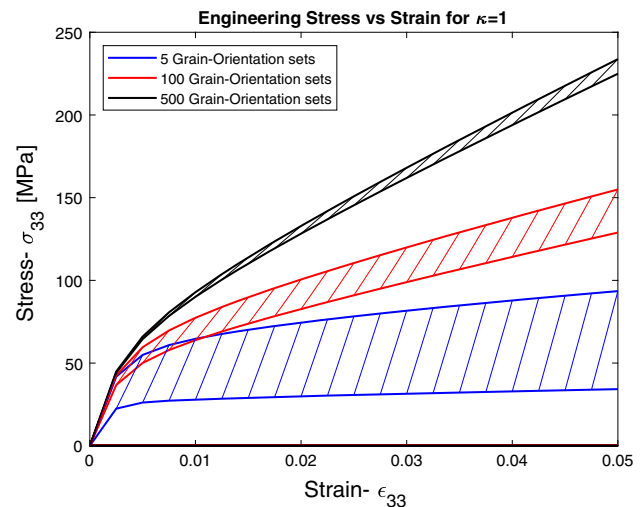


Fig. 14 Engineering stress versus strain responses for specimens with different 5, 100 and 500 randomly oriented grains using a constant grain boundary strength $\kappa = 1$

cases, resulting in more pronounced hardening behavior. In one single plot various microstructural effects are illustrated in a very simple way in Fig. 14. In Fig. 15 the spatial stress evolution is shown for the case with symmetry boundary conditions with $\kappa = 16$ and $m = 0.2$, where the response of the same specimen with $12.5 \times 50 \mu\text{m}$ (left) and $25 \times 100 \mu\text{m}$

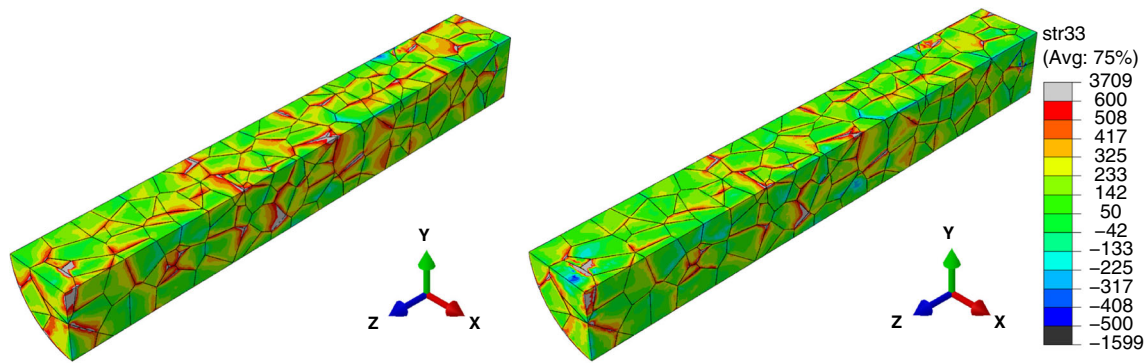


Fig. 15 Stress distribution for the small $12.5 \times 50 \mu\text{m}$ (left) and large $25 \times 100 \mu\text{m}$ (right) specimens using $\kappa = 16$ and $m = 0.2$ including 252 grains under 1% tensile strain in z-direction

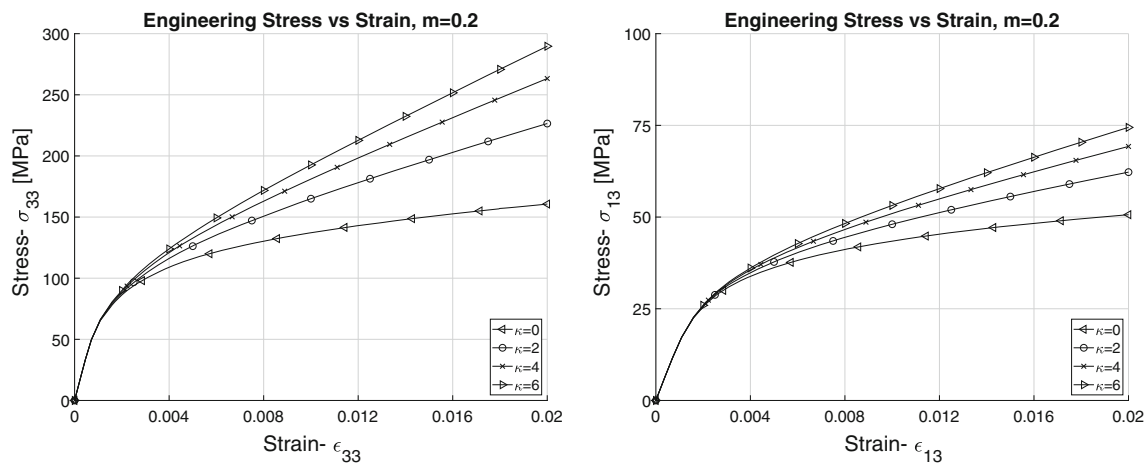


Fig. 16 Engineering stress versus strain response for a 100 grain $25 \times 25 \mu\text{m}$ specimen through different grain boundary strength κ values in comparison to classical grain boundary conditions for $m = 0.2$ under axial loading (left) and shear loading (right)

(right) dimensions are compared. As expected the case with small grain size shows higher stress concentrations at the grain boundaries, which would start softening first and fails with a smaller toughness value.

In the last example the response of a shorter specimen with $25 \mu\text{m}$ length and $25 \mu\text{m}$ diameter, including 100 randomly oriented grains is addressed under both uni-axial tensile and shear loading considering different κ values of 0, 2 and 6 with $m = 0.2$. First, the stress versus strain responses are shown in Fig. 16. As expected, the macroscopic stress levels are lower in shear case compared to the axial loading one and even though the same trend is obtained with increasing κ the effect is more pronounced in the axial loading case. The von Mises stress contour plots are presented in Fig. 17 for $\kappa = 0, 2, 6$. The magnitude of stress concentration is much lower in the shear case and the inter-granular stress evolution is completely different between the two loading scenarios. In both cases an increase in grain boundary stresses is clearly observed due to the increase in κ .

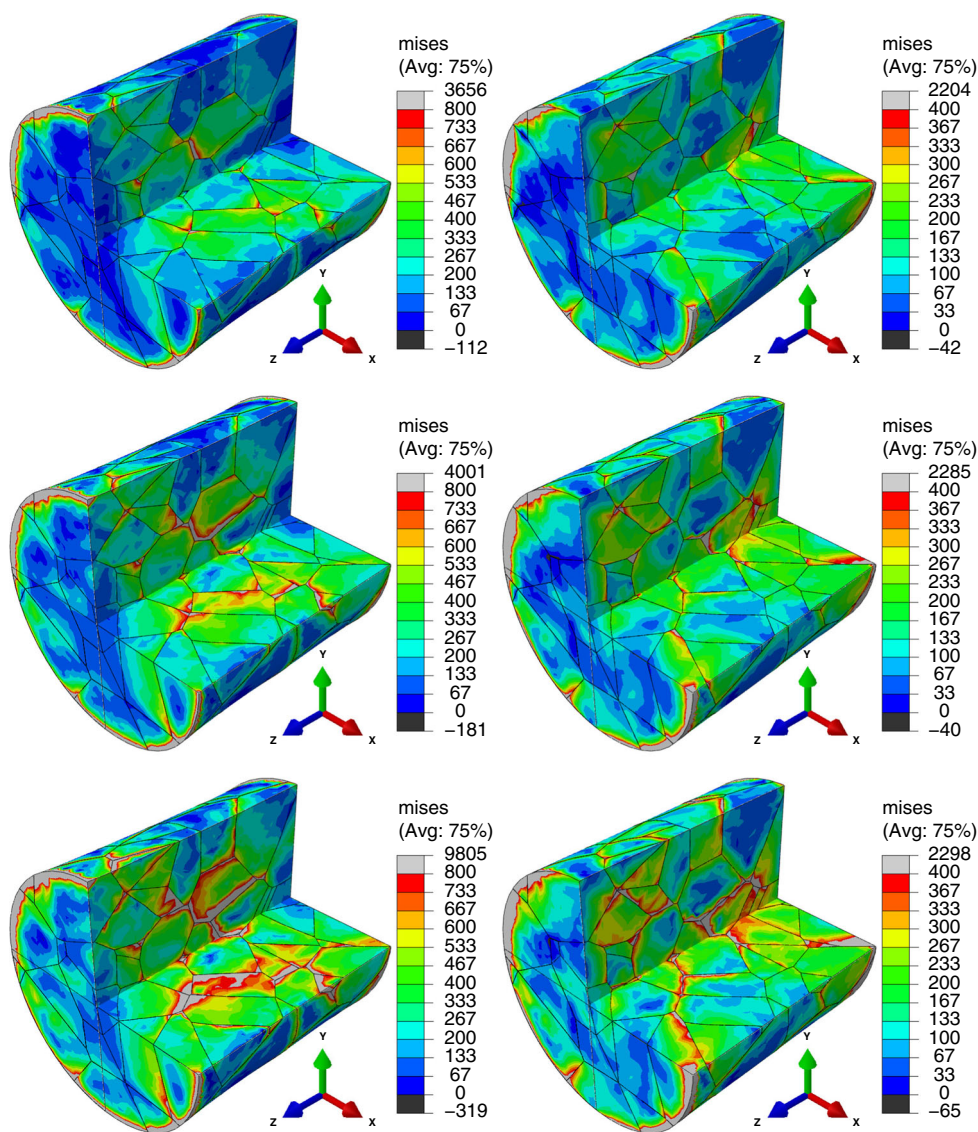
The computations presented in this paper are conducted using desktop computers. The simulations with the model

including 10 grains where $m = 0.1$ take 2–3 h to complete depending on the κ value through 14,339 finite elements and 81,271 DOFs on a PC with Intel Xeon E5 1650 v4 3.60 GHz CPU and 72 GB RAM using single thread. The sample with 100 grains includes 85,251 finite elements and 423,101 DOFs and takes 40–50 h to complete depending on the κ value on the same PC. On the other hand using $m = 1$ increases the speed substantially reducing the 10 grain computation time to 20–30 min. For example the sample with 600 grains having 486,014 finite elements and 2,309,043 DOFs takes around 20 h to complete using $m = 1$.

5 Conclusions

This work presents a detailed evaluation of three dimensional microstructure evolution and constitutive response of micron-sized polycrystalline specimens through a strain gradient crystal plasticity framework incorporating Gurtin’s grain boundary model. The mis-orientation and grain boundary orientation dependent intergranular localization is stud-

Fig. 17 The von Mises stress distribution for axial loading (left) and shear loading (right) in specimens with 100 randomly oriented grains for $m = 0.2$ under 2% tensile and shear strain. Grain boundary strength values are: $\kappa = 0$ (top), $\kappa = 2$ (middle), $\kappa = 6$ (bottom)



ied through the framework reflecting the coarse grained representation of complex grain boundary-dislocation slip interaction mechanisms. The illustrations from the current model go beyond the capacity of classical strain gradient crystal plasticity frameworks which could illustrate the plasticity activity at the grain boundaries through solely limiting soft (micro-free) and hard (micro-clamped) boundary conditions. The real situations that would be in between these two limiting cases are captured here through the developed framework with the help of the grain boundary strength parameter which magnifies the effect of misorientation between the neighboring grains. The macroscopic constitutive response approaches to the limiting cases for the low and high values of the interface strength respectively. A detailed boundary condition analysis is presented, which is crucial for the understanding of capacity of local and non-local crystal plasticity

frameworks. The results are in agreement with the theoretical expectations of the grain boundary model that has been developed on geometrical arguments. The microstructure evolution and the macroscopic constitutive response are addressed through different microstructural parameters together with the intrinsic and extrinsic size effects in polycrystalline materials. The effect of crystal orientation distribution, which change the stress concentration evolution completely, is illustrated as well. The study presents a great potential for capturing the experimental microstructure evolution and macroscopic response due to the degree of freedom introduced by the GB model, which is quite problematic for the problems with large number of grains. Therefore, the outlook would be an experimental comparison and validation study of microstructure evolution in polycrystalline metallic alloys.

Acknowledgements Tuncay Yalçinkaya gratefully acknowledges the support by the Scientific and Technological Research Council of Turkey (TÜBİTAK) under the 3501 Programme (Grant No. 117M106).

Compliance with ethical standards

Conflict of interest The authors declare that they have no conflict of interest.

References

- Geiger M, Kleiner M, Eckstein R, Tiesler N, Engel U (2001) Microforming. *CIRP Ann* 50(2):445–462
- Vollertsen F, Schulze Niehoff H, Hu Z (2006) State of the art in micro forming. *Int J Mach Tools Manuf* 46(11):1172–1179
- Abuzaid WZ, Sangid MG, Carroll JD, Sehitoglu H, Lambros J (2012) Slip transfer and plastic strain accumulation across grain boundaries in hastelloy x. *J Mech Phys Solids* 60(6):1201–1220
- Bieler TR, Eisenlohr P, Roters F, Kumar D, Mason DE, Crimp MA, Raabe D (2009) The role of heterogeneous deformation on damage nucleation at grain boundaries in single phase metals. *Int J Plast* 25(9):1655–1683
- Guery A, Hild F, Latourte F, Roux S (2016) Slip activities in polycrystals determined by coupling dic measurements with crystal plasticity calculations. *Int J Plast* 81:249–266
- Guo Y, Britton TB, Wilkinson AJ (2014) Slip band-grain boundary interactions in commercial-purity titanium. *Acta Mater* 76:1–12
- Yalçinkaya T (2017) Strain gradient crystal plasticity: thermodynamics and implementation. In: Voyiadjis G (ed) *Handbook of nonlocal continuum mechanics for materials and structures*. Springer, Cham, pp 1–32
- Yalçinkaya T, Özdemir I, Firat AO, Tandogan IT (2018b) Micromechanical modeling of inter-granular localization, damage and fracture. *Procedia Struct Integr* 13:385–390
- Yalçinkaya T, Özdemir I, Simonovski I (2018c) Micromechanical modeling of intrinsic and specimen size effects in microforming. *Int J Mater Form* 11:729–741
- Yalçinkaya T, Özdemir I, Firat AO (2019) Inter-granular cracking through strain gradient crystal plasticity and cohesive zone modeling approaches. *Theor Appl Fract Mech* 103:102306
- Güler B, Simsek Ü, Yalçinkaya T, Efe M (2018) Grain-scale investigations of deformation heterogeneities in aluminum alloys. *AIP Conf Proc* 1960:170005
- Ma A, Roters F, Raabe D (2006) On the consideration of interactions between dislocations and grain boundaries in crystal plasticity finite element modeling - theory, experiments, and simulations. *Acta Mater* 54(8):2181–2194
- Ng KS, Ngan AHW (2009) Deformation of micron-sized aluminium bi-crystal pillars. *Philos Mag* 89(33):3013–3026
- Zaefferer S, Kuo JC, Zhao Z, Winning M, Raabe D (2003) On the influence of the grain boundary misorientation on the plastic deformation of aluminum bicrystals. *Acta Mater* 51:4719–4735
- Zhao Z, Ramesh M, Raabe D, Cuitino AM, Radovitzky R (2008) Investigation of three-dimensional aspects of grain-scale plastic surface deformation of an aluminum oligocrystal. *Int J Plast* 24(12):2278–2297
- Zhang Z, Lunt D, Abdolvand H, Wilkinson AJ, Preuss M, Dunne FPE (2018) Quantitative investigation of micro slip and localization in polycrystalline materials under uniaxial tension. *Int J Plast* 108:88–106
- Lim H, Carroll JD, Corbett CB, Boyce BL, Weinberger CR (2015) Quantitative comparison between experimental measurements and cp-fem predictions of plastic deformation in a tantalum oligocrystal. *Int J Mech Sci* 92:98–108
- Acar P, Ramazani A, Sundararaghavan V (2017) Crystal plasticity modeling and experimental validation with an orientation distribution function for ti-7al alloy. *Metals* 7(11):459
- Doquet V, Barkia B (2016) Combined AFM, SEM and crystal plasticity analysis of grain boundary sliding in titanium at room temperature. *Mech Mater* 103:18–27
- Liang H, Dunne FPE (2009) Gnd accumulation in bi-crystal deformation: crystal plasticity analysis and comparison with experiments. *Int J Mech Sci* 51:326–333
- Mello AW, Nicolas A, Lebensohn RA, Sangid MD (2016) Effect of microstructure on strain localization in a 7050 aluminum alloy: comparison of experiments and modeling for various textures. *Mater Sci Eng A* 661:187–197
- Pinna C, Lan Y, Kiu MF, Efthymiadis P, Lopez-Pedrosa M, Farrugia D (2015) Assessment of crystal plasticity finite element simulations of the hot deformation of metals from local strain and orientation measurements. *Int J Plast* 73:24–38
- Sachtleber M, Zhao Z, Raabe D (2002) Experimental investigation of plastic grain interaction. *Mater Sci Eng A* 336(1):81–87
- Tasan CC, Hoefnagels JPM, Diehl M, Yan D, Roters F, Raabe R (2014) Strain localization and damage in dual phase steels investigated by coupled in-situ deformation experiments and crystal plasticity simulations. *Int J Plast* 63:198–210
- Roters F (2005) Application of crystal plasticity fem from single crystal to bulk polycrystal. *Comput Mater Sci* 32(3):509–517
- Luccarelli PG, Pataky GJ, Sehitoglu H, Foletti S (2017) Finite element simulation of single crystal and polycrystalline haynes 230 specimens. *Int J Solids Struct* 115–116(3):270–278
- Gurtin ME (2008) A theory of grain boundaries that accounts automatically for grain misorientation and grain-boundary orientation. *J Mech Phys Solids* 56:640–662
- Özdemir I, Yalçinkaya T (2014) Modeling of dislocation-grain boundary interactions in a strain gradient crystal plasticity framework. *Comput Mech* 54:255–268
- Yalçinkaya T, Brekelmans WAM, Geers MGD (2012) Non-convex rate dependent strain gradient crystal plasticity and deformation patterning. *Int J Solids Struct* 49:2625–2636
- Yalçinkaya T, Brekelmans WAM, Geers MGD (2011) Deformation patterning driven by rate dependent non-convex strain gradient plasticity. *J Mech Phys Solids* 59:1–17
- Özdemir I, Yalçinkaya T (2017) Strain gradient crystal plasticity: intergranular microstructure formation. In: Voyiadjis G (eds) *Handbook of nonlocal continuum mechanics for materials and structures*, pp 1035–1065
- van Beers PRM, McShane GJ, Kouznetsova VG, Geers MGD (2013) Grain boundary interface mechanics in strain gradient crystal plasticity. *J Mech Phys Solids* 61(12):2659–2679
- van Beers PRM, Kouznetsova VG, Geers MGD, Tschopp MA, McDowell DL (2015) A multiscale model of grain boundary structure and energy: from atomistics to a continuum description. *Acta Mater* 82(12):513–529
- Gottschalk D, McBride A, Reddy BD, Javili A, Wriggers P, Hirschberger CB (2016) Computational and theoretical aspects of a grain-boundary model that accounts for grain misorientation and grain-boundary orientation. *Comput Mater Sci* 111:443–459
- Bayerschen E, McBride AT, Reddy BD, Böhlke T (2016) Review on slip transmission criteria in experiments and crystal plasticity models. *J Mater Sci* 51(5):2243–2258
- Alipour A, Reese S, Wulfinghoff S (2019) A grain boundary model for gradient-extended geometrically nonlinear crystal plasticity: theory and numerics. *Int J Plast* 118:17–35
- Wulfinghoff S (2017) A generalized cohesive zone model and a grain boundary yield criterion for gradient plasticity derived from surface- and interface-related arguments. *Int J Plast* 92:57–78

38. Evers LP, Brekelmans WAM, Geers MGG (2004b) Non-local crystal plasticity model with intrinsic ssd and gnd effects. *J Mech Phys Solids* 52:2379–2401
39. Klusemann B, Yalcinkaya T (2013) Plastic deformation induced microstructure evolution through gradient enhanced crystal plasticity based on a non-convex helmholtz energy. *Int J Plast* 48:168–188
40. Rys M, Petryk H (2018) Gradient crystal plasticity models with a natural length scale in the hardening law. *Int J Plast* 111:168–187
41. Bittencourt E (2019) Interpretation of the size effects in micropillar compression by a strain gradient crystal plasticity theory. *Int J Plast* 116:280–296
42. Kuroda M (2017) Interfacial microscopic boundary conditions associated with backstress-based higher-order gradient crystal plasticity theory. *J Mech Mater Struct* 12:193–218
43. Spannraft L, Ekh M, Larsson F, Runesson K, Steinmann P (2020) Grain boundary interaction based on gradient crystal inelasticity and decohesion. *Comput Mater Sci* 178:109604
44. Gurtin ME (2000) On the plasticity of single crystals: free energy, microforces, plastic-strain gradients. *J Mech Phys Solids* 48:989–1036
45. Gurtin ME (2002) A gradient theory of single-crystal viscoplasticity that accounts for geometrically necessary dislocations. *J Mech Phys Solids* 50:5–32
46. Arsenlis A, Parks DM, Becker R, Bulatov VV (2004) On the evolution of crystallographic dislocation density in non-homogeneously deforming crystals. *J Mech Phys Solids* 52:1213–1246
47. Bayley CJ, Brekelmans WAM, Geers MGD (2006) A comparison of dislocation induced back stress formulations in strain gradient crystal plasticity. *Int J Solids Struct* 43:7268–7286
48. Evers LP, Brekelmans WAM, Geers MGD (2004a) Scale dependent crystal plasticity framework with dislocation density and grain boundary effects. *Int J Solids Struct* 41:5209–5230
49. Yefimov S, Groma I, van der Giessen E (2004) A comparison of a statistical-mechanics based plasticity model with discrete dislocation plasticity calculations. *J Mech Phys Solids* 52:279–300
50. Yalcinkaya T, Özdemir I, Firat AO (2018a) Three dimensional grain boundary modeling in polycrystalline plasticity. *AIP Conf Proc* 1960:170019
51. Huang Y (1991) A user-material subroutine incorporating single crystal plasticity in the abaqus finite element program: mech. report 178. Technical Report, Division of Engineering and Applied Sciences, Harvard University, Cambridge, Massachusetts
52. Kysar JW (1997) Addendum to a user-material subroutine incorporating single crystal plasticity in the abaqus finite element program: mech. report 178. Technical Report, Division of Engineering and Applied Sciences, Harvard University, Cambridge, Massachusetts
53. Acharya A, Bassani JL (2000) Lattice incompatibility and a gradient theory of crystal plasticity. *J Mech Phys Solids* 48:156–1595
54. Dunne FPE, Rugg D, Walker A (2007) Lengthscale-dependent, elastically anisotropic, physically-based hcp crystal plasticity: Application to cold-dwell fatigue in ti alloys. *Int J Plast* 23:1061–1083
55. Han CS, Gao H, Huang Y, Nix WD (2005a) Mechanism-based strain gradient crystal plasticity–i. theory. *J Mech Phys Solids* 53:1188–1203
56. Han CS, Gao H, Huang Y, Nix WD (2005b) Mechanism-based strain gradient crystal plasticity–ii. analysis. *J Mech Phys Solids* 53:1204–1222
57. Borg U (2007) A strain gradient crystal plasticity analysis of grain size effects in polycrystals. *Eur J Mech A Solid* 26:313–324
58. Klusemann B, Yalcinkaya T, Geers MGD, Svendsen B (2013) Application of non-convex rate dependent gradient plasticity to the modeling and simulation of inelastic microstructure development and inhomogeneous material behavior. *Comput Mater Sci* 80:51–60
59. Bargmann S, Ekh M, Runesson K, Svendsen B (2010) Modeling of polycrystals with gradient crystal plasticity: a comparison of strategies. *Philos Mag* 90:1263–1288
60. Bittencourt E, Needleman A, Gurtin ME, Van der Giessen E (2003) A comparison of nonlocal continuum and discrete dislocation plasticity predictions. *J Mech Phys Solids* 51:281–310
61. Ekh M, Grymer M, Runesson K, Svedberg T (2007) Gradient crystal plasticity as part of the computational modelling of polycrystals. *Int J Numer Methods Eng* 72:197–220
62. Okumura D, Higashi Y, Sumida K, Ohno N (2007) A homogenization theory of strain gradient single crystal plasticity and its finite element discretization. *Int J Plast* 23:1148–1166

Publisher's Note Springer Nature remains neutral with regard to jurisdictional claims in published maps and institutional affiliations.